Optical and electrical features of calcium molybdate scheelite solar cells

das Neves Stigger, Ananda Ramires ; Fonseca Hernandes, V.; Meneghetti Ferrer, Mateus ; Lucio Moreira, Mario

DOI
10.1039/d3nj01434g

Publication date
2023

Document Version
Final published version

Published in
New Journal of Chemistry

NJC

ROYAL SOCIETY OF CHEMISTRY

PAPER

View Article Online
View Journal

Cite this: DOI: 10.1039/d3nj01434g

Optical and electrical features of calcium molybdate scheelite solar cells

Ananda Ramires das Neves Stigger, *[a] Vinicius Fonseca Hernandes,[ac] Mateus Meneghetti Ferrer[b] and Mario Lucio Moreira [ab]

Received 28th March 2023,
Accepted 24th May 2023

DOI: 10.1039/d3nj01434g

rsc.li/njc

Calcium molybdate (CMO) is a material used in several technological applications. In this work, we explored the correlation between the optical and electrical properties of CMO in solar cell photoanodes. Six samples were prepared by a microwave-assisted hydrothermal method with pH values of 4, 7, and 10 associated with temperatures of 100 °C and 140 °C. These samples were used as a replacement for titanium dioxide TiO_2 in Graetzel solar cells. A thin blocking layer (BL), a dense and translucent film, was deposited over a CMO layer using a doctor-blade method, to create a heterojunction. We show that a strict correlation between pH, temperature, processing time, and photovoltaic response exists in CMO scheelite and needs to be considered to achieve optimal photovoltaic behavior. Almost all samples achieved typical solar cell responses, except that synthesized with pH 4 at 100 °C, which shows an anomalous behavior. Among these samples, the one synthesized with pH 10 at 100 °C was identified as the most suitable candidate for down-converter materials in solar energy applications, due to its typical diode-like properties, with an upper J_{sc} = 180 μA cm^{-2}, V_{oc} = 607 mV and FF = 0.45.

Introduction

Studies that bring innovations to the renewable energy sector have been essential in helping combat climate change, as reported in ref. 1. Hydroelectric plants have the largest participation in renewable energy generation in the world, providing more than 16.6% of total global electricity.[2] Moreover, the transformation of wind into electric energy is a relatively recent process and not well spread throughout the world.[3] The need for renewable energy sources brought great attention to photovoltaic technologies, which use energy from the sun to produce electricity. Until this moment, the most important barrier in solar cells is their low energy-conversion power. This creates a demand for new, more efficient materials, to be implemented as photovoltaic devices.[4] O'Regan and Graetzel were pioneers in the study of dye-sensitized solar cells (DSSC) using low-cost materials and processes. In this type of cell, a TiO_2 layer is used to generate a photocurrent, with electrons photoexcited from dye and injected directly in the conduction band of TiO_2.[5–7] These cells are considered hybrid cells, because they are made with inorganic and organic materials and are typically used as semiconductor materials in photoanodes, dye-sensitizers, electrolytes, and cathode photo-electrochemicals.[8]

The application of materials, such as $SrTiO_3$, $CaTiO_3$, and $BaTiO_3$ perovskites,[9] and optimized methods, for the improvement of film layers and interface engineering, have been greatly contributing to the third-generation photovoltaic field.[10] Perovskite solar cells, in particular, have received great attention due to their high-power outputs and low production costs,[11] showing electrical, optical, and conduction properties very suitable for this application.[12]

Another group of materials that have been used for optoelectronic applications is the scheelite group, which can be excited by visible light irradiation, due to great absorption capability and high electron mobility. Typically, scheelites have an ABO_4 composition, where A = Ca or Pb, and B = Mo or W, originating families of molybdate and tungstate groups of materials with interesting structural and luminescence properties.[13] In this context, the luminescence of calcium molybdate arises as a new perspective for solar cell applications.[14]

The aim of this work is to prepare CMO samples by hydrothermal methods and apply these compounds in solar cells. To achieve this, two steps are required: the CMO synthesis, with two main parameters established, pH and temperature of synthesis, and the preparation of the solar cells. This study reports the relationship of pH and temperature to CMO samples applied in photoanode solar cells. To better comprehend this correlation of pH and temperature of synthesis to the resulting CMO properties, a theoretical approach using density functional theory was also utilized.

[a] Post-Graduate Program in Physics, Federal University of Pelotas, 96160-000, Capão do Leão, RS, Brazil. E-mail: anandaramires@gmail.com
[b] Post-Graduate Program in Materials Science and Engineering, Federal University of Pelotas, 96010-610, Pelotas, RS, Brazil
[c] Kavli Institute of Nanoscience, Delft University of Tecnology, 2628CJ Delft, The Netherlands

Experimental

In this work, six samples of calcium molybdate were prepared and applied as photoanodes in solar cells. Synthesis parameters, such as pH and temperature, were investigated. Specifically, three samples were prepared at 100 °C and pH 4, 7, and 10, and three others at 140 °C and pH 4, 7, and 10. All samples used the same base (precursors and solvents); however, to reach the desired pH, additional elements were sometimes added to the precursor solution. The detailed process is described below.

CMO preparation

At first, a precursor solution of 0.01 mol of sodium molybdate bihydrate in 40 ml of distilled water was vigorously stirred with a magnetic bar for 15 min at room temperature. Concomitantly, 0.01 mol of calcium nitrate was mixed in 40 ml distilled water and kept under constant magnetic stirring for 15 min. After homogenization, the two solutions were transferred to the same beaker (mixed) and kept under constant magnetic stirring for 30 min. To adjust the pH, 0.11 ml of nitric acid was added to each sample, to achieve pH = 4, and 0.24 ml of potassium hydroxide was added to achieve pH = 10. In both cases, the concentration was kept at 0.01 mol. After the pH-agent introduction, the new precursor solutions were kept under constant magnetic stirring for 15 min. After homogenization, each solution was transferred to a microwave oven adapted for hydrothermal synthesis (800 W, working frequency 2.45 GHz) and the reaction was performed at 100 °C or 140 °C, for 40 minutes. After hydrothermalization, the precipitate was separated from the solution *via* centrifuging, and washed until a neutral pH (~7) was reached. The final material was dried at 100 °C for 12 h. Fig. 1 shows an illustration of this process. This process is as per the literature.[15]

Block layer preparation

Initially, FTOs were cleaned using three steps of sonification, containing 1 v/v detergent, deionized water, and ethanol, for 10 min for each process. Before deposition, FTOs were also immersed in ethanol at 80 °C. The titanium solution was prepared with 0.366 ml of isopropoxide bis(acetylacetonate) of titanium and 2.134 ml of iso-propanol. Then, the solution was deposited on the FTO substrate in two steps, using the spin coating methodology, the first step at 1500 rpm for 15 seconds, and second step at 3000 rpm for 30 seconds, with the atmospheric humidity below 55%. Finally, a heat treatment was performed at 125 °C for 10 minutes and subsequently at 500 °C for 30 minutes.[16]

Solar cell fabrication

The solar cell is made of two main parts: the negative and the positive electrodes. The positive part is composed of the heterojunction of two films: a first layer of TiO_2 (block layer, described above) and a second layer of calcium molybdate. The preparation of the CMO film consists of paste made by mixing 60 mg of the powder with 20 μl of ethylene glycol, 20 μl of Triton-X100 and 20 μl of ethanol. Afterward, the mixture is kept under magnetic stirring until the required viscosity is achieved. The deposition of the CMO pastes is performed using a doctor-blade method. Specifically, tape is used to delimit an area of 1 cm^2 where the solution paste is deposited. This methodology also allows the determination of the film thickness. After the deposition, the sample is dried at room temperature and the substrate with the deposited film is taken into a muffle, to be heat-treated at two different temperatures, first 125 °C for 6 minutes and then 500 °C for 30 minutes. The negative electrode is prepared with two layers of platinum and deposited *via* thermal decomposition. After the electrodes are prepared, the solar cell is mounted as demonstrated in Fig. 2, sealed, and an electrolyte formed from potassium iodide/triiodide is introduced. This process is the same as that used in ref. 17.

Characterization techniques

The CMO crystals were structurally characterized by X-ray diffraction (XRD) using a Rigaku diffractometer with Cu-K radiation from 20° to 120° with a 0.02° step width and a scanning rate of 5 s for each point. The shape and the self-organization of the particles were investigated by scanning electron microscopy images using field emission scanning electron microscopy (FE-SEM, Zeiss Supra TM 35). Raman spectroscopy was used to determine the short-range order of the powders; the equipment used was a Bruker FT-Raman (Fourier transform Raman), model RFS100S with a 1064 nm wavelength Nd:YAG laser with 4 cm^1 spectral resolution and 100 mW power. The optical gap

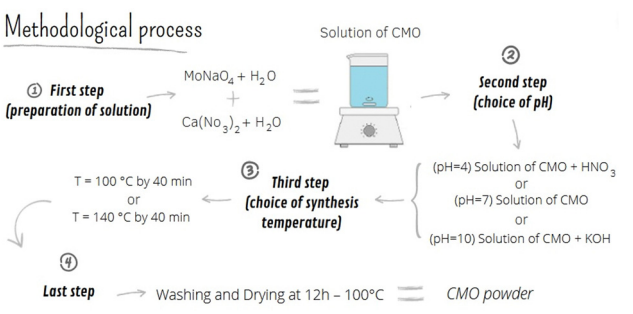

Fig. 1 Schematic diagram describing the methodological process to obtain CMO powders.

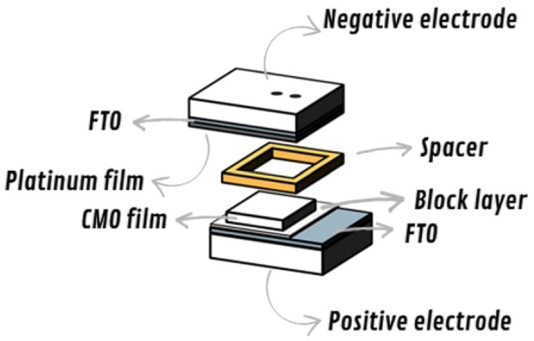

Fig. 2 Schematic diagram of the solar cell fabrication process, pointing out each element of the cell.

was measured using UV-Vis light absorption spectroscopy in diffuse reflectance mode, using a Cary 5000 spectrophotometer, in the range from 200 to 800 nm, from which the direct band gap is calculated using the Wood and Tauc method. The photoluminescence spectrum was obtained in the range of 350 to 1200 nm using a Thermo Jarrell-Ash Monospec 27 monochromator and a Hamamatsu 446 photomultiplier. The characteristic photovoltaic *J–V* curve of solar cells was measured using a AMETK VERSASTAT3 potentiostat, in the range of 600 mV to −100 mV, in a solar simulator SLB-300A ScienceTech under AM1.5G illumination and 100 mW cm^{-2} of irradiance at 25 °C.

Theoretical section

Calculations for the CMO were performed within a periodic density functional theory framework, using the CRYSTAL17 package.[18] The atomic centers of Ca, Mo, and O have been described by 86-511d21G,[19] 311(d31)G,[20] and 8411(d11)[21] basis sets, respectively, taken from the CRYSTAL website.[22] Becke's three-parameter hybrid nonlocal exchange functional[23] was used in combination with a Lee–Yang–Parr gradient-corrected correlation functional.[24] Thresholds controlling the accuracy of the calculation of the Coulomb and exchange integrals were set to 10^{-8} (ITOL1 to ITOL4) and 10^{-16} (ITOL5) and the percent of Fock/Kohn–Sham matrix mixing was set to 40 (IPMIX = 40). The band structure and Raman vibrational modes, accompanied by respective frequencies, were calculated using the CRYSTAL17 package.

Results and discussion

Characterization of powder

Fig. 3a shows the X-ray diffraction (XRD) patterns for the calcium molybdate powders, synthesized at 100 °C with three different pH values (4, 7, and 10), all being indexed as a tetragonal structure with space group $I41/a$, with cell constants a = 5.22 Å and c = 11.42 Å, according to the ICSD-62219 and literature.[25] The absence of additional peaks, associated with low width to half height, indicates that the pure single phase and a good degree of crystallization have been obtained. However, the main peak at 2θ = 28.5°, relative to the (112) plane, shown in detail in Fig. 3b, registers the displacement caused by the synthesis pH, a low angle displacement showing crystalline plane expansion.

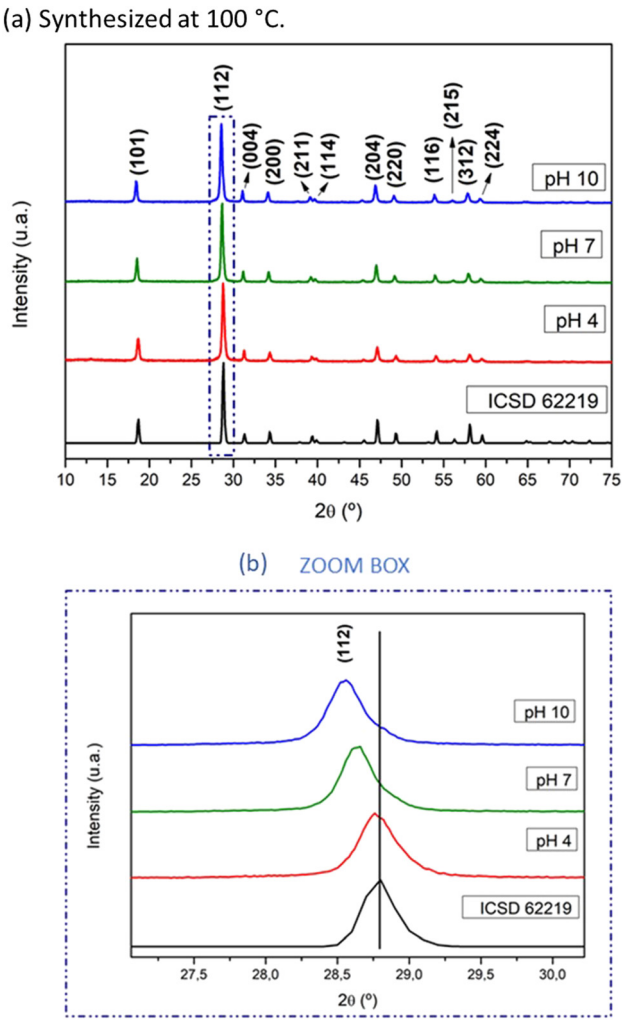

Fig. 3 XRD patterns of the samples synthesized at 100 °C. (a) Samples with pH 4, 7, and 10 and (b) zoomed plots of the range close to the (112) peak.

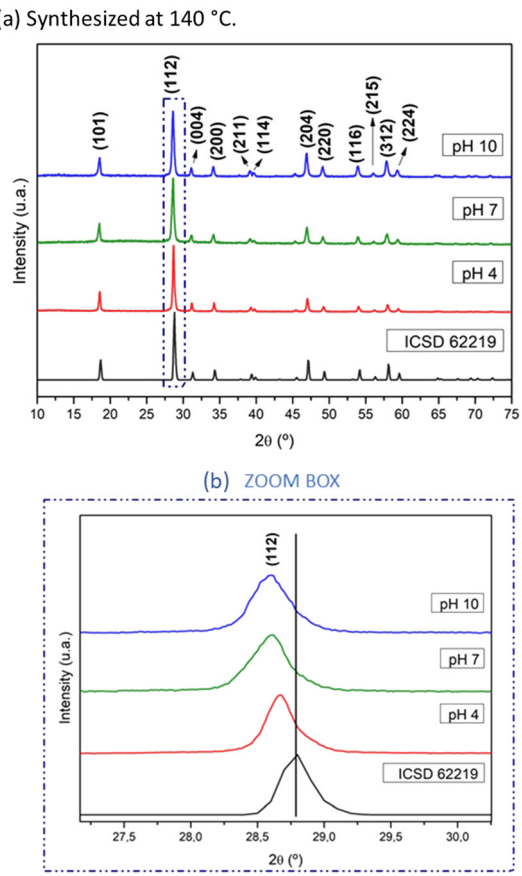

Fig. 4 XRD patterns of the sample synthesized at 140 °C. (a) Samples with pH 4, 7, and 10 and (b) zoomed plot of the range close to the (112) peak.

Table 1 Rietveld refinement, with A and C being the lattice parameters

Sample	A (Å)	C (Å)	Volume (Å^3)	X^2	R-Bragg	Displacement ($28.5°(2\theta)$)
pH 4 at 100 °C	5.227	11.449	312.802	1.067	0.209	0.02
pH 4 at 140 °C	5.229	11.448	312.991	1.112	0.073	0.13
pH 7 at 100 °C	5.230	11.443	312.950	1.042	0.099	0.16
pH 7 at 140 °C	5.232	11.449	313.387	1.209	0.096	0.19
pH 10 at 100 °C	5.231	11.444	313.186	1.120	0.078	0.25
pH 10 at 140 °C	5.236	11.458	314.177	1.216	0.089	0.19

Similar to the samples synthesized at 100 °C, the samples synthesized at 140 °C showed the same phase indexed with crystallographic ICSD-62219 – Fig. 4a. However, a larger displacement is noticeable, Fig. 4b, when compared to the previous case. Thus, we found that independent of the temperature of synthesis used, the CMO samples showed good crystallization and the formation of pure phases. Moreover, the displacement indicates an expansion of the lattice with the increase of pH, a behavior even more evident with Rietveld refinement, as indicated in Table 1.

Rietveld refinement confirms the unit cell expansion, from 312.802 A^3 to 314.177 A^3. This expansion was observed in both lattice parameters, with A and C growing from 5.227 Å to 5.236 Å, and from 11.449 Å to 11.458 Å, respectively. The displacement of the samples' most intense peak, regarding crystallographic record, is observed for the majority of cases, which indicated a homogeneous traction defect. The phenomenon is not observed in the sample with pH 4, synthesized at 100 °C, which shows a very low displacement, as shown in Table 1. The reliability of this result is supported by optimal R-Bragg and χ^2 parameters, close to 0 and 1, respectively. The former corresponds to the difference between the intensity of

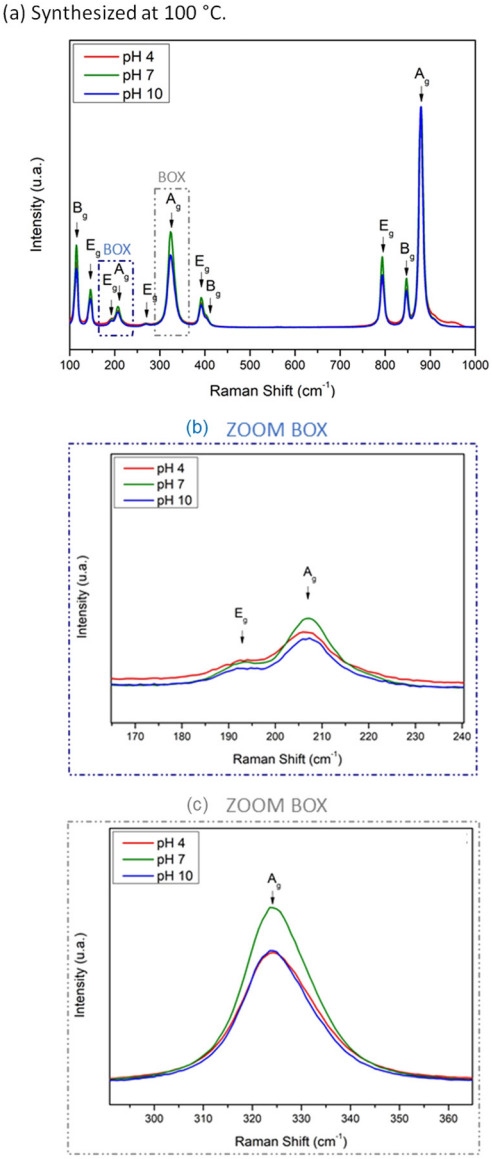

Fig. 5 Raman spectroscopy of samples synthesized at 100 °C, (a) samples with pH 4, 7 and 10, (b) zoomed-in box of modes E_g and A_g, and (c) zoomed-in box of mode A_g.

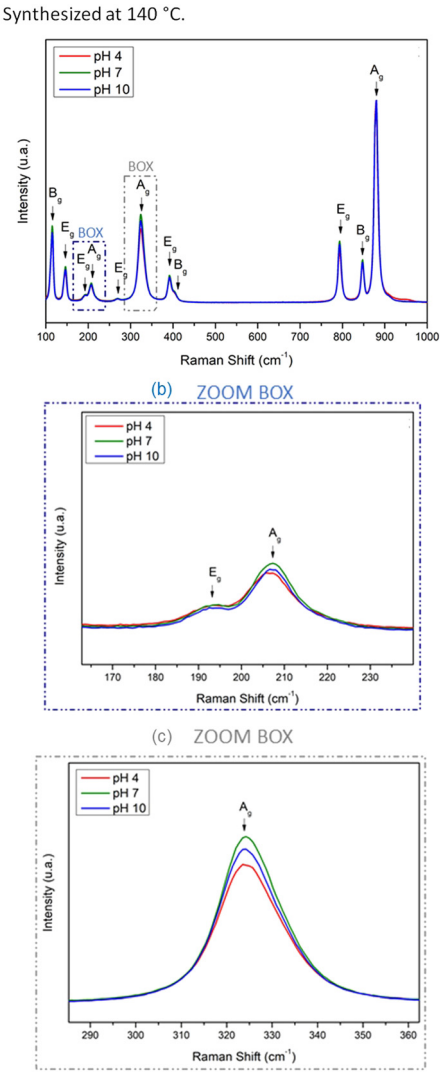

Fig. 6 Raman spectroscopy of samples synthesized at 140 °C, (a) samples with pH 4, 7, and 10, (b) zoomed-in box of modes E_g and A_g and (c) zoomed-in box of mode A_g.

the calculated and the experimental peaks, with an optimal value equal to zero. The latter determines the convergence of refinement, defined by the ratio between the experimental and the calculated diffraction. For the sample with pH 4 synthesized at 100 °C, the *R*-Bragg value was the worse overall, indicating that the main diffraction peak was less displaced in the sample with pH 4 synthesized at 100 °C, compared to the sample synthesized with pH 10 at 100 °C, which has a larger X^2 value.

From Raman spectroscopy, 11 vibrational modes were identified. Fig. 5 and 6 show this characterization; all spectra were normalized. It is possible to verify from the Raman spectrum that CMO belongs to the scheelite crystal group according to the literature[26] and with our calculated vibrational modes.

The group of scheelite cells have 26 different vibration modes; however, only A_g, B_g, and E_g are Raman active.[27] The theoretical analysis developed by Oliveira *et al.* shows that six of these modes ($1A_g + 2B_g + 3E_g$) are external pure lattice modes of the tetrahedral MoO_4 cluster, while the other seven ($2A_g + 3B_g + 2E_g$) are internal motions of tetrahedral MoO_4 clusters and octahedral CaO_8 clusters.[28]

In our study, all the samples show 11 Raman active modes, however, two modes were not observed, which may be undetected due to the low intensity when compared to the main detected modes. Simulated Raman active modes, obtained using the CRYSTAL17 package, can be seen in Table 2, with 11 modes corresponding to the measured modes. The frequencies obtained in our simulation allow us to characterize the atoms related to each vibrational mode and show good correspondence with previous studies of the material.[27–29] Fig. 5b and 6b show that the modes at 192 cm^{-1} and 207 cm^{-1} present different intensities for both temperatures of 100 °C and 140 °C, probably caused by the modification of the pH values of the synthesis. These vibrations are correlated with Ca–Ca stretching, and thus an intensity change indicates an increase of tension at this vibration.

In the mode located at 325 cm^{-1} highlighted in the zoom boxes in Fig. 5 and 6, a direct correlation between the vibrational intensity and pH of synthesis is observed. These specific vibrational modes are identified as Ca–O and Mo–O internal modes, as described in Table 2. The same behavior is observed for modes around 200 cm^{-1}, also related to Ca–O and Mo–O vibrations in these cases. All the structures are more tensioned.

Fig. 7 and 8 show the UV-vis curves of the calcium olybdate sample, which were calculated using the equation based on the methodology proposed by Wood and Tauc.[30] Each energy gap value was determined by the linear extrapolation of the linear section on the absorption spectrum of the curve through a line that intercepts the energy axis to estimate the band gap value. The Wood and Tauc model considers that the tail of the state, even when having a low rate of transmission, still contributes to

Table 2 Raman active vibrational modes calculated using the CRYSTAL17 package. Types of vibration: (B) bending, (S) stretch and (O) others

Raman active modes (cm^{-1})	Irreducible repr.	Type of vibration and participating atoms
119.83	(B_g)	(B) O–Ca–O
147.37	(E_g)	(B) Ca–Ca–Ca (B) Ca–Ca–O
179.92	(E_g)	(B) Ca–Ca–O (B) Ca–Ca–Ca
201.40	(B_g)	(S) Ca–Ca–Ca
208.15	(A_g)	(B) O–Ca–O (B) O–Mo–O
270.42	(E_g)	(S) O–Ca–Ca (B) O–Mo–O
320.97	(B_g)	(S) Ca–O–Mo (S) O–Ca–Ca
324.55	(A_g)	(S) O–Ca–Ca (B) O–Ca–Ca (B) O–MO–O
398.47	(E_g)	(O) O–Mo–O
406.03	(B_g)	(B) O–Ca–O (B) O–Ca–Ca (O) O–MO–O
787.34	(E_g)	(S) O–Mo
840.61	(B_g)	(S) O–Mo
875.64	(A_g)	(B) Ca–O–Mo (B) O–Ca–Ca (S) O–MO

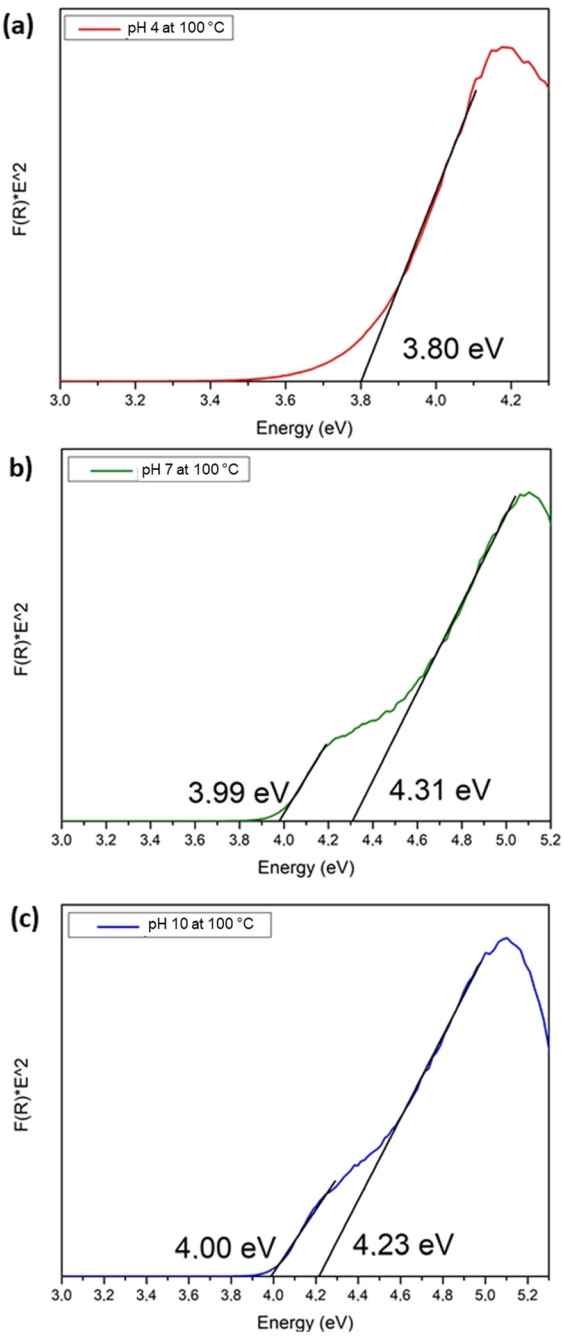

Fig. 7 UV-visible spectra of samples synthesized at 100 °C: (a) sample with pH 4, (b) sample with pH 7, and (c) sample with pH 10.

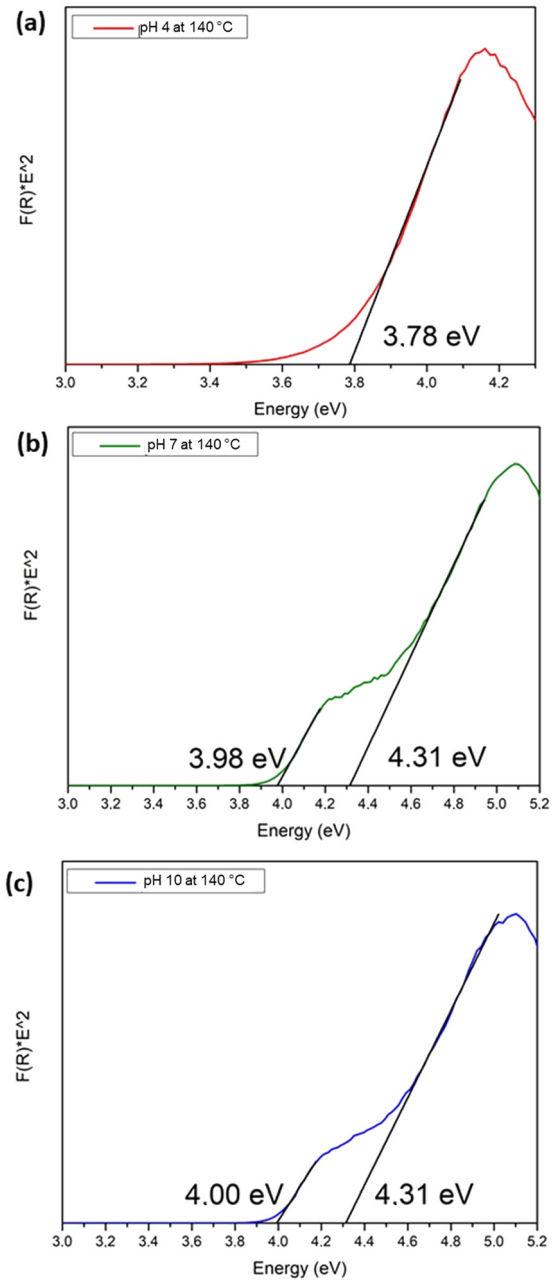

Fig. 8 UV-visible spectra of samples synthesized at 140 °C: (a) sample with pH 4, (b) sample with pH 7, and (c) sample with pH 10.

the process, thus showing the existence of more than one preference transmission, as shown in Fig. 7b and c. Samples with pH 4, and temperatures of 100 °C and 140 °C, have only one absorption located at 3.8 eV, which is in accordance with the literature.[31] Although the other samples, namely those with pH 7 and 10, show two absorptions, indicating the multi-absorption process and hence a double gap, the first one is located approximately at 4.3 eV and the second at approximately 4.0 eV. This behavior is probably engendered by the pH of synthesis, becoming very important to our application in solar cells. CMO has a very high band gap energy for this application, where normally materials with an energy gap close

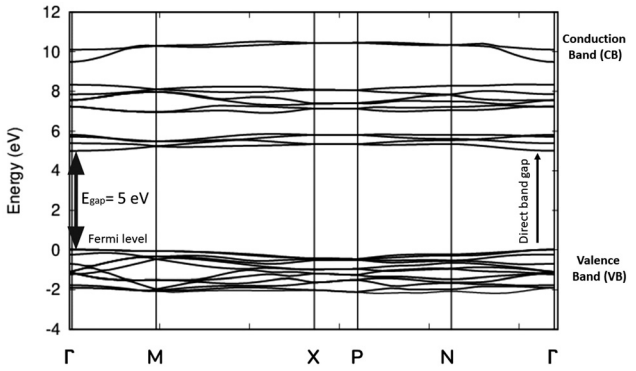

Fig. 9 Band structure for CMO.

to 3.2 eV are used.[8] The emergence of intermediate stages works as a "step" process, where absorptions occur in subsequent stages by charge transfer among gaps through alignment of internal gaps, as a result of a new specific band structure.

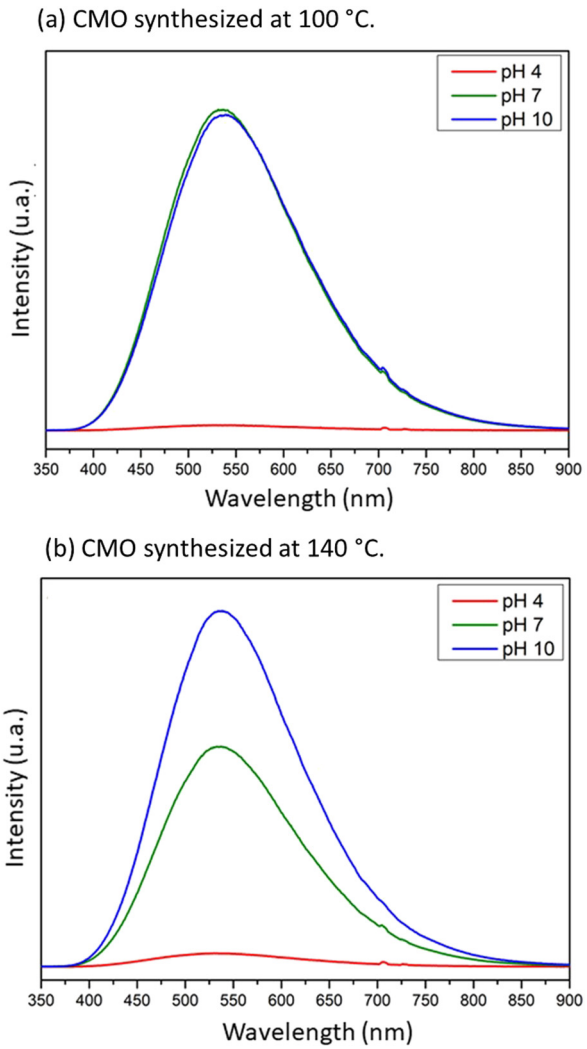

Fig. 10 Photoluminescence of CMO powders synthesized at temperatures of (a) 100 °C at pH values of 4, 7, and 10 and (b) 140 °C at pH values of 4, 7, and 10.

To corroborate the experimental gaps, Fig. 9 shows the band structure for CMO, calculated using the CRYSTAL17 package, from which we can see that the maximum of the valence band and the minimum of the conduction band are both located at the Γ point, which indicates that CMO presents a direct transition, with a band gap energy equal to 5 eV. The simulated material's band structure results show good correspondence with the literature,[25] with a band gap energy slightly higher than the experimental value found in this and other works.[28] Unfortunately, our simulation was unable to show the localized states in the band gap. Moreover, the reduction of the band gap value corroborated the arousing of new states closer to the conduction band (deep states).

With the intent of better comprehension of the absorption process, the results of the photoluminescence (PL) emission spectra of the CMO particles with pH values of 4, 7, and 10 synthesized at 100 °C and 140 °C are shown in Fig. 10. It is possible to observe a broad emission band that covers the range of 400–800 nm for samples with pH 7 and 10, at both temperatures of synthesis, while any emission was obtained for samples with pH 4, the peak maximum of it is related to oxygen vacancies and particle size in the lattice.[32,33]

One interesting point of this result is about our potential application of CMO as a photoanode in solar cells. The sample synthesized with pH 4 reports anomalous behavior, which will be better explained in the photovoltaic section. This same sample does not have photoluminescence emissions, and its band gap is 3.8 eV, in accordance with the largest band gap among the samples of this work. Moreover, the samples synthesized with pH 7 and 10 have luminescence emissions, but also show a double gap. In both cases, important conditions to get a photoanode are satisfied: for the pH 4 samples, the absence of luminescence, and for samples with pH 7 and 10, the double gap absorption process. The profile of the emission is the same as shown by Longo *et al.*, where the emission band is typical of a multiphonon and multilevel process, involving the participation of numerous states within the band gap of the material.[34]

Fig. 11 shows the SEM micrographs of CMO crystals as described above. The morphological study is important and fundamental to understanding the shape, size, and agglomeration formation. For all samples, mesocrystal features were obtained, which correspond to oriented growth. However, the nanocrystals remain as individual particles, all with approximately the same size of around 100 nm, forming mesocrystals with approximately 2 μm;[35] it is important that the particle sizes were not changed for all pH values used in the synthesis, keeping the individual particle around 100 nm for all cases. This characteristic is important for the application in solar cells because the material has a higher contact surface with the electrolytes, making it easier for it to become the charge transporter.

The formation of mesocrystals is evidenced by the highly magnified images of Fig. 11 and 12 (100 °C and 140 °C samples on the right columns), obtained from the dotted set out areas of the original images (left columns of 100 °C and 140 °C samples, Fig. 11 and 12).

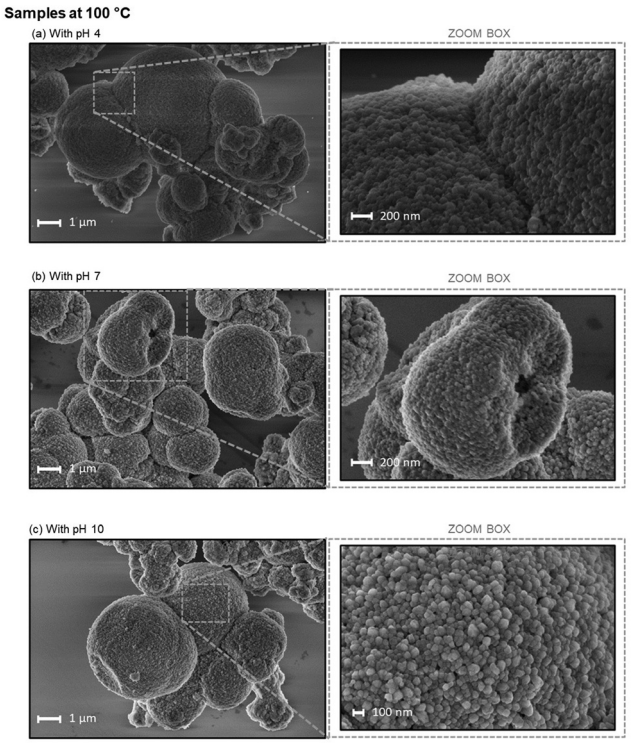

Fig. 11 SEM images of samples synthesized at 100 °C, (a) with pH 4, (b) with pH 7, and (c) with pH 10.

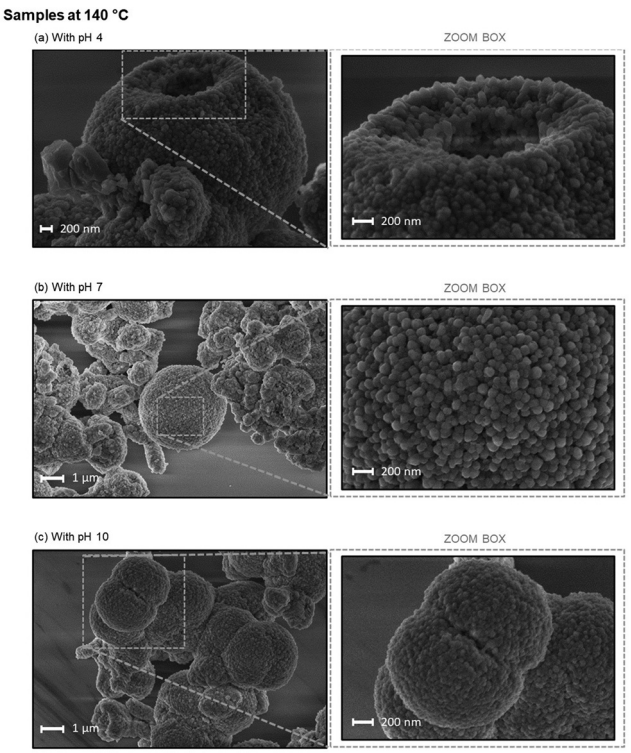

Fig. 12 SEM images of samples synthesized at 140 °C, (a) with pH 4, (b) with pH 7, and (c) with pH 10.

Photovoltaic behavior

In Fig. 13 and 14, the typical photovoltaic curves *J vs. V* measured by symmetric potential (−5 to 5 V) are presented for all samples. It is important to note that all samples were measured without dye (very important to Graetzels solar cells) even then all show photovoltaic behavior, except pH 4 samples that report an anomalous behavior. The increase of photocurrent density as the voltage increases looks like an ohmic behavior, but this is broken at 350 mV when the photocurrent starts to decrease quickly. This probably is governed by grain border outlines, which act initially as a potential barrier in a resistive circuit and at 350 mV become a trapper of charges. Thus, these samples will not be considered for photoanodes in solar cells.

In solar cell devices, it is necessary to apply a symmetric potential, so that photon incidence can be converted into a current, which is possible because the photoluminescence

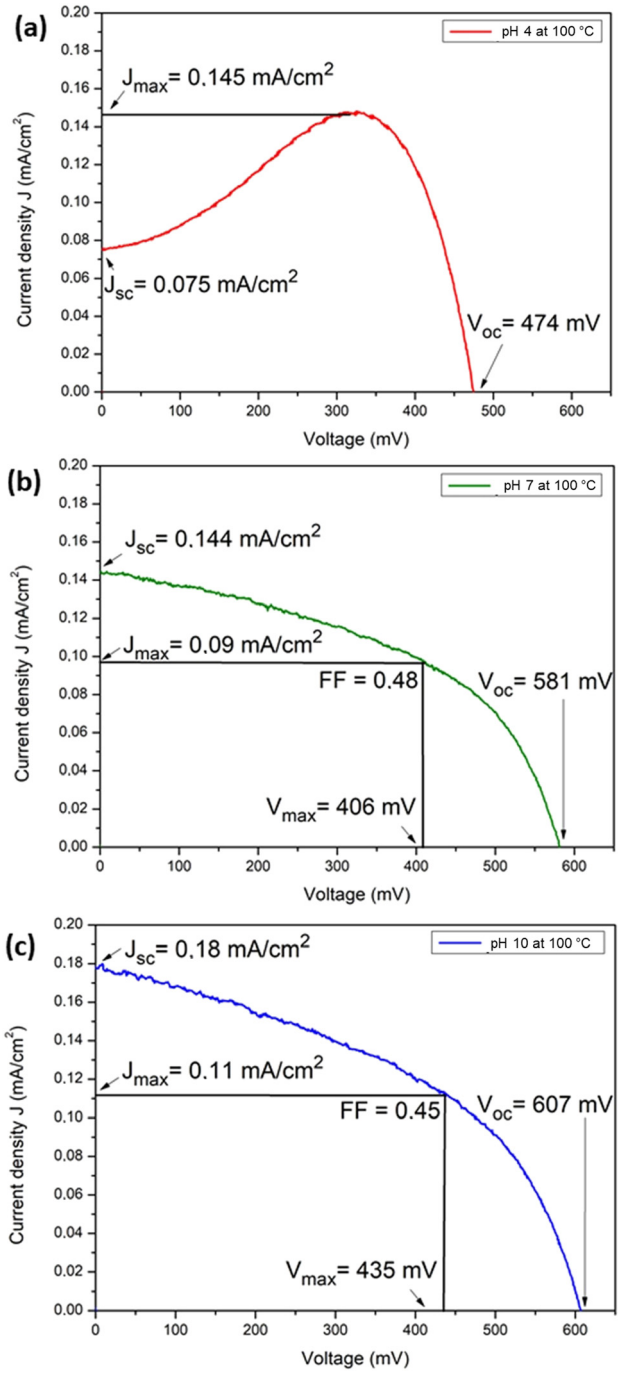

Fig. 13 Photovoltaic behavior of the samples synthesized at 100 °C, (a) with pH 4, (b) with pH 7, and (c) with pH 10.

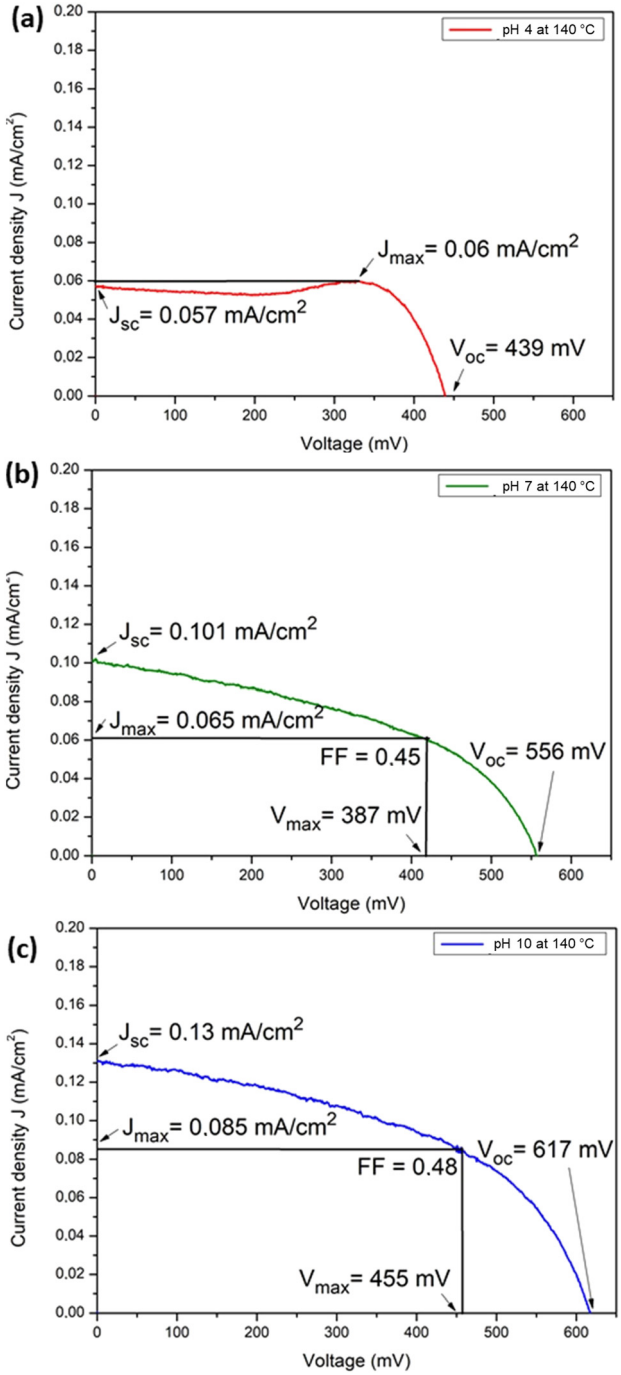

Fig. 14 Photovoltaic behavior of the samples synthesized at 140 °C, (a) with pH 4, (b) with pH 7, and (c) with pH 10.

Table 3 Results of the V_{oc}, J_{sc}, V_{max}, J_{max}, FF and η solar cell's CMO

Samples	V_{oc} (mV)	J_{sc} (mA cm^{-2})	V_{max} (mV)	J_{max} (mA cm^{-2})	FF	η
pH 4 at 100 °C	474	0.075	—	0.145	—	—
pH 7 at 100 °C	581	0.144	406	0.090	0.48	0.401
pH 10 at 100 °C	607	0.180	435	0.110	0.45	0.491
pH 4 at 140 °C	439	0.057	—	0.060	—	—
pH 7 at 140 °C	556	0.010	387	0.065	0.45	0.252
pH 10 at 140 °C	617	0.130	455	0.085	0.48	0.385

properties of CMO materials stabilized excited electrons that do not decay and contribute to photocurrent generation. Table 3 shows the results of the CMO cells. The solar cell with pH 4 at 100 °C does not show typical behavior, with the highest J_{max} among all samples, 0.145 mA cm^{-2}; however it is impossible to calculate FF. The cells with pH 10 at 100 °C showed the best photovoltaic performance amongst all samples, with values of J_{sc} (mA cm^{-2}) = 0.180 (mA cm^{-2}), V_{oc} = 607 mV, η equals 0.49 and FF = 0.45.

Conclusions

In summary, calcium molybdate has been successfully synthesized by a microwave-assisted hydrothermal method. By adjusting the pH of synthesis, we could obtain different properties for the same material. The photovoltaic behavior with the increase of pH in the calcium molybdate synthesis caused structural distortions, which were fundamental for our application. We observed that, independently of the pH and temperature of synthesis, all samples showed a crystalline structure; however, the PL showed a difference between samples, which is essential to this application. Although the efficiency was still low when compared to typical TiO_2 DSSCs, the control of photovoltaic behavior was not previously observed for this material, opening an opportunity to apply this methodology to other systems.

Conflicts of interest

There are no conflicts to declare.

Acknowledgements

The authors wish to thank Brazilian financial support agencies: Coordenação de Aperfeiçoamento de Pessoal de Nível Superior – Brasil (CAPES), Conselho Nacional de Desenvolvimento Científico e Tecnológico (CNPq) and FAPERGS – Process no. 17/2551-0000889-8 and 19/2551-0001974-2. The authors also gratefully acknowledge the laboratories: CCAF/UFPel, Materials Optical Spectroscopy Center CEOMAT/UFRGS, Interdisciplinary Laboratory of Electrochemistry and Ceramics/UFSCar for giving space for the characterization and preparation of the samples for this work.

Notes and references

1 F. Zhang, *et al.*, Inter-sector network and clean energy innovation: Evidence from the wind power sector, *J. Cleaner Prod.*, 2020, **263**, 121287.
2 M. Bilgili, *et al.*, The role of hydropower installations for sustainable energy development in Turkey and the word., *Renewable Energy*, 2018, **126**, 755–764.
3 M. T. Tolmasquim, *Energia renovável: hidráulica, biomassa, eólica, solar, oceânica*, EPE, Rio de Janeiro, 2016, vol. 1.1, p. 10.
4 J. A. Castillo-Robles, *et al.*, Advances on Dye-Sensitized Solar Cells (DSSCs) Nanostructures and Natural Colorants: A Review, *J. Compos. Sci.*, 2021, **5**(11), 288.
5 M. Kim, *et al.*, Conformal quantum dot–SnO2 layers as electron transporters for efficient perovskite solar cells, *Science*, 2022, **375**(6578), 302–306.
6 S. Sánchez, *et al.*, Thermally controlled growth of photoactive FAPbI 3 films for highly stable perovskite solar cells, *Energy Environ. Sci.*, 2022, **15**(9), 3862–3876.
7 J. Cao and F. Yan, Recent progress in tin-based perovskite solar cells, *Energy Environ. Sci.*, 2021, **14**(3), 1286–1325.
8 B. O'regan and M. Grätzel, A low-cost, high-efficiency solar cell based on dye-sensitized colloidal TiO2 films, *Nature*, 1991, **353**(6346), 737–740.
9 Y. Okamoto and Y. Suzuki, Perovskite-type SrTiO3, CaTiO3 and BaTiO3 porous film electrodes for dye-sensitized solar cells, *J. Ceram. Soc. Jpn.*, 2014, **122**(1428), 728–731.
10 Y. Liu and Y. Chen, Integrated Perovskite/Bulk-Heterojunction Organic Solar Cells, *Adv. Mater.*, 2020, **32**(3), 1805843.
11 M. Saliba, Perovskite solar cells must come of age, *Science*, 2018, **359**(6374), 388–389.
12 S. Borbón, *et al.*, ZnTiO3 nanoparticles for application as photoanode in dye-sensitized solar cells (DSSC), *Phys. B*, 2022, **630**, 413704.
13 C. Tablero, Optical absorption and applications of the ABO4 (A = Ca, Pb and B = Mo, W) semiconductors, *Chem. Phys. Lett.*, 2015, **635**, 190–195.
14 A. Verma and S. K. Sharma, Dual-mode luminescence: a new perspective in calcium molybdate phosphor for solar cell application, *J. Mater. Sci.: Mater. Electron.*, 2019, **30**(12), 11778–11789.
15 G. Botelho, *et al.*, Study of structural and optical properties of CaMoO4 nanoparticles synthesized by the microwave-assisted solvothermal method, *Mater. Chem. Phys.*, 2016, **183**, 110–120.
16 T. S. Lilge, *et al.*, Increase of V_{oc} using heterojunctions of BaTiO3 without sensitization, *Ceram. Int.*, 2020, **46**(4), 4907–4913.
17 C. D. Fernandes, *et al.*, An investigation of the photovoltaic parameters of ZnS grown on ZnO (101 [combining macron] 1), *New J. Chem.*, 2020, **44**(47), 20600–20609.
18 R. Dovesi, *et al.*, Quantum-mechanical condensed matter simulations with CRYSTAL, *Wiley Interdiscip. Rev.: Comput. Mol. Sci.*, 2018, **8**(4), e1360.
19 L. Valenzano, *et al.*, Ab initio study of the vibrational spectrum and related properties of crystalline compounds; the case of $CaCO_3$ calcite, *Z. Phys. Chem.*, 2006, 893–912.

20 F. Corà, *et al.*, Anab initio Hartree–Fock study of α-MoO3, *J. Mater. Chem.*, 1997, **7**(6), 959–967.
21 E. Heifets, *et al.*, Thermodynamic stability of non-stoichiometric SrFeO 3− δ: a hybrid DFT study, *Phys. Chem. Chem. Phys.*, 2019, **21**(7), 3918–3931.
22 CRYSTAL, **https://www.crystal.unito.it/basis-sets.php**.
23 A. D. Becke, Density-functional thermochemistry. III. The role of exact exchange, *J. Chem. Phys.*, 1993, **98**, 5648–5652.
24 C. Lee, W. Yang and R. G. Parr, Development of the Colle-Salvetti correlation-energy formula into a functional of the electron density, *Phys. Rev. B: Condens. Matter Mater. Phys.*, 1988, **37**(2), 785.
25 M. Minakshi, *et al.*, Phase evolution in calcium molybdate nanoparticles as a function of synthesis temperature and its electrochemical effect on energy storage, *Nanoscale Adv.*, 2019, **1**(2), 565–580.
26 D. Christofilos, G. A. Kourouklis and S. Ves, A high-pressure Raman study of calcium molybdate, *J. Phys. Chem. Solids*, 1995, **56**(8), 1125–1129.
27 A. P. A. Marques, *et al.*, Evolution of photoluminescence as a function of the structural order or disorder in $CaMoO_4$ nanopowders, *J. Appl. Phys.*, 2008, **104**(4), 043505.
28 F. K. F. Oliveira, *et al.*, Experimental and theoretical study to explain the morphology of $CaMoO_4$ crystals, *J. Phys. Chem. Solids*, 2018, **114**, 141–152.
29 S. P. S. Porto and J. F. Scott, Raman Spectra of CaWO4, SrWO4, $CaMoO_4$, and $SrMoO_4$, *Phys. Rev.*, 1967, **157**(3), 716.
30 J. Tauc, R. Grigorovici and A. Vancu, Optical properties and electronic structure of amorphous germanium, *Phys. Status Solidi B*, 1966, **15**(2), 627–637.
31 M. Ghaed-Amini, M. Bazarganipour and M. Salavati-Niasari, Calcium molybdate octahedral nanostructures, hierarchical self-assemblies controllable synthesis by coprecipitation method: characterization and optical properties, *J. Ind. Eng. Chem.*, 2015, **21**, 1089–1097.
32 K. G. Sharma and N. R. Singh, Synthesis and luminescence properties of $CaMO_4$:Dy^{3+} (M = W, Mo) nanoparticles prepared via an ethylene glycol route, *New J. Chem.*, 2013, **37**(9), 2784–2791.
33 S. Sinha, *et al.*, Enhancement of upconversion, temperature sensing and cathodoluminescence in the K^+/Na^+ compensated $CaMoO_4$:Er^{3+}/Yb^{3+} nanophosphor, *New J. Chem.*, 2017, **41**(13), 5362–5372.
34 V. M. Longo, *et al.*, Different origins of green-light photoluminescence emission in structurally ordered and disordered powders of calcium molybdate, *J. Phys. Chem. A*, 2008, **112**(38), 8920–8928.
35 L. Zhou and P. O'Brien, Mesocrystals: a new class of solid materials, *Small*, 2008, **4**(10), 1566–1574.

